Spontaneous Electrochemical Reconstruction of NiNb2O6@C for High-Rate Lithium-Ion Batteries

Peer-reviewed author version

Tan, Lidan; Zhou, Sheng; Jin, Yi; Zhu , Hui; Zhang, Qin; Guo, Jianguang; Li, Xuanke; Dong, Zhijun; YANG, Nianjun & Cong, Ye (2024) Spontaneous Electrochemical Reconstruction of NiNb2O6@C for High-Rate Lithium-Ion Batteries. In: Chemical engineering journal (1996. Print), 495 (Art N° 153397).

DOI: 10.1016/j.cej.2024.153397
Handle: http://hdl.handle.net/1942/43405

Spontaneous Electrochemical Reconstruction of $NiNb_2O_6$@C for High-Rate Lithium-Ion Batteries

Lidan Tan[a], Sheng Zhou[a], Yi Jin[b], Hui Zhu[a], Qin Zhang[a], Jianguang Guo[a], Xuanke Li[a], Zhijun Dong[a], Nianjun Yang[c,d,*], Ye Cong[a,*]

[a]*The State Key Laboratory of Refractories and Metallurgy, Hubei Province Key Laboratory of Coal Conversion and New Carbon Materials, Wuhan University of Science and Technology, Wuhan, 430081, P. R. China*

[b]*Key Laboratory for Polymerization Engineering and Technology of Ningbo, School of Materials Science and Chemical Engineering, Ningbo University of Technology (NBUT), Ningbo 315016, P. R. China*

[c]*Institute of Materials Engineering, University of Siegen, 57076, Siegen, Germany*

[d]*Department of Chemistry, IMO-IMOMEC, Hasselt University, 3590, Diepenbeek, Belgium*

ABSTRACT

Niobium oxides are widely active in the arena of lithium-ion batteries due to their distinctive structure and rapid charging capability, nevertheless facing the serious challenge from their inherently low electrical conductivity. Herein, a molten salt method is proposed to prepare nickel niobate ($NiNb_2O_6$) anode materials for lithium-ion batteries, and a carbon coating derived from mesophase pitch is fabricated to construct $NiNb_2O_6$@C composites. Importantly, $NiNb_2O_6$@C undergoes spontaneous electrochemical reconstruction to generate metallic Ni and amorphous Nb_2O_5 during the initial charge/discharge cycle. The presence of the outer carbon layer not only serves as a uniform conductive coating to improve the conductivity and thereby deliver superior rate performance, but also effectively inhibits the stripping of Ni^0 to guarantee a great cycling stability. The synergistic effects of the dual conductive interfaces,

* Corresponding authors.

E-mail addresses: congye@wust.edu.cn (Y. Cong); nianjun.yang@uhasselt.be (N. Yang).

consisting of the carbon layer and the Mott-Schottky heterojunction between amorphous Nb_2O_5 and metallic Ni, culminate in exceptional electrochemical performance. Specifically, $NiNb_2O_6$@C-10% delivers impressive specific capacity of 436.3 mAh g^{-1} at 0.5 C and conspicuous cycling stability, maintaining 86.3% capacity retention after 800 cycles at 10 C. This work underscores the substantial potential of nickel niobate anode materials in advancing the development of next-generation lithium-ion batteries.

Keywords: Nickel niobate; Carbon coating; Electrochemical reconstruction; Anode; Lithium-ion battery

1. Introduction

Nowadays, with the rapid development of electronic products, electric vehicles and electrical power grids, efficient energy storage equipment is playing an increasingly important role. Different electronic products have various requirements for energy storage devices. For example, portable electronic products demand high theoretical capacity, mechanical reliability, and high safety of batteries. Electric vehicle batteries need to satisfy the characteristics of high energy density and rapid rechargeability [1-4]. Lithium-ion batteries (LIBs) have become the most widely used energy storage devices due to their high energy density, low self-discharge effect, strong security, portability, and many other advantages. Finding appropriate anode materials is one of the crucial factors to enhance the properties of LIBs [5-8]. Graphite, as the most widely commercialized anode material for LIBs, also has unavoidable disadvantages. A case in point is graphite may form lithium dendrites at low operating voltages, leading to diaphragm damage and battery short circuit [9, 10]. By contrast, $Li_4Ti_5O_{12}$ exhibits high safety and “zero strain” characteristics, so it has occupied one seat in the anode materials of LIBs. However, its low theoretical capacity (175 mAh g^{-1}) largely limits future development [11, 12]. Therefore, it is urgent to explore a convenient, low-cost, energy-saving, and mass-production preparation method to prepare a new generation

of lithium-ion battery anode materials.

Niobium-based oxides, as a new type of intercalation/deintercalation materials, have high lithium intercalation potential and high specific capacity due to their multivalent characteristics [13, 14]. The research of niobium-based oxides provides more choices for the development of energy storage equipment. Up to now, niobium-based oxides such as Nb_2O_5 [15-19], $TiNb_2O_7$ [20-24], $Ti_2Nb_{10}O_{29}$ [25-29], $Cu_2Nb_{34}O_{87}$ [30, 31], have been extensively studied and applied to various energy storage devices.

Recently, a new niobium-based oxide electrode material, nickel niobate ($NiNb_2O_6$), has caught our attention. Its unique crystal structure provides a single type of channels for Li^+ intercalation, which is more conducive to the transportation and storage of lithium ions. As a results, $NiNb_2O_6$ exhibits outstanding rate performance and cycle life performance. Xia et al. has demonstrated $NiNb_2O_6$ as a new high-performance anode material for lithium-ion batteries, which was synthesized using the traditional solid-state method at 1150 °C [32]. To reduce the cost of energy requirements, Zhang et al. proposed a mechanically assisted solid-state method, which can prepare pure $NiNb_2O_6$ material at 900 °C [33]. Furthermore, hydrothermal methods have also been adopted to successfully synthesize the nickel niobate anode material, which unfortunately is a cumbersome process unsuitable for large-scale industrial production [34]. Compared with the conventional solid-state reaction process, molten salt synthesis is a simple, highly repeatable, green, and safe preparation method. The reaction environment of melting at high temperature helps to reduce the kinetic restriction of the reactions, and promote the diffusion and reactions of reactants. It offers the advantages of low synthesis temperature, short reaction time, uniform chemical composition, high purity, small particle sizes and so on [35]. A recent work has successfully prepared submicron $NiNb_2O_6$ particles using the molten salt method at 900 °C [36].

Unfortunately, the advantages of this preparation method are difficult to fundamentally solve the inherent low conductivity problem of niobium-based oxides. Therefore, it is extremely necessary to develop other modification strategies to improve the conductivity of $NiNb_2O_6$, such as carbon coating, introduction of heteroatoms and establishment special structure [37]. Due to their high conductivity, carbon materials

are usually used to modify oxides and form conductive coating on the surface to accelerate the rapid transmission of electron/ion between electrode materials. In the selection of carbon materials, we follow the principles of high conductivity, stable structure and low cost and so on [38, 39]. Mesophase pitch, a typical carbonaceous mesophase raw material, has the advantages of high residual carbon yield, high electrical conductivity, strong processability and easy graphitization, also has a wide range of sources and low price, therefore it is recognized as an ideal precursor of carbon coating materials [40].

In addition, an interesting phenomenon is found that divalent metal will undergo reduction to form zero-valent metal in some niobium-based composite metal oxides. Zhai et al. proposed mulberry-like $Sn_2Nb_2O_7/SnO_2$ nanoparticles as an anode material for SIBs, in which a large number of Sn nanodots are reduced and well embedded in an amorphous $Na_xNb_2O_5$ substrate after the first cycle [41]. Moreover, Zhang et al. found a similar phenomenon in $NiNb_2O_6$ as an anode material for LIBs [34]. Ni metal is replaced by Li to form $Li_xNb_2O_5$ after the first charge/discharge cycle, and Ni metal no longer participated in the subsequent electrochemical reactions. This phenomenon of metal reduction can play important roles in improving electrical conductivity. Recent studies have demonstrated that the morphological evolution derived from electrochemical activation, sintering, and reconstruction during electrochemical reactions may optimize properties, owing to the formation of defect structures or heterostructures, the exposure of more active sites and the generation of more ion diffusion channels.

In this work, we presented a novel approach for fabricating $NiNb_2O_6$-based composites as anode materials for LIBs using the molten salt method, which can achieve the synthesis of $NiNb_2O_6$ at lower temperature and the preparation of nanomaterial without additional nanocrystallization. A carbon layer derived from mesophase pitch coated on $NiNb_2O_6$ particles enables to enhance the conductivity and electrochemical properties of the composite. Most importantly, owing to the electrochemical reconstruction of $NiNb_2O_6$ during the initial charge and discharge process, a unique Mott-Schottky heterostructure composed of amorphous Nb_2O_5 and

Ni^0 metal is constructed. This structure facilitates rapid charge transfer, thereby enhancing electron transport dynamics during lithium storage. The carbon layer also acts as a protective barrier for Ni^0 metal to inhibit the detachment of Ni^0 from the material surface, further enhancing the electronic conductivity of the material. Owing to the synergistic effects of carbon layer and Mott-Schottky heterojunction generated from the electrochemical reconstruction process, the $NiNb_2O_6$@C-10% anode exhibits a striking specific capacity of 436.3 mAh g^{-1} at 0.5 C, and a desirable capacity retention of 86.3% after 800 cycles at 10 C. When assembled into a full cell, the capacity can achieve 85.5 mAh g^{-1} at 5 C after 500 cycles.

2. Experimental Section

2.1 Chemicals

Nickel oxide (NiO, AR, 99.9%) and niobium oxide (Nb_2O_5, AR, 99.9%) were purchased from Shanghai Macklin Biochemical Co., Ltd. Nickel chloride ($NiCl_2 \cdot xH_2O$, AR, 98%) was obtained from Aladdin Biochemical Technology Co., Ltd. Potassium chloride (KCl, AR, 99.5%), Sodium chloride (NaCl, AR, 99.5%) and ethanol absolute (C_2H_6O, AR, 99.7%) were sourced from Sinopharm Chemical Reagent Co., Ltd. All the reagents were used without any purifications.

2.2 Materials Preparation

2.2.1 Preparation of $NiNb_2O_6$

The $NiNb_2O_6$ was synthesized using a modified molten salt method. In this process, nickel oxide (NiO) and niobium oxide (Nb_2O_5) powders in a molar ratio of 1: 1 were mixed with an inorganic salt media composed of NaCl, KCl and $NiCl_2$ in a of 0.45: 0.45: 0.1 molar ratio. The weight ratio of metal oxides and inorganic salts was 1: 5. Subsequently, the mixture with ethanol was stirred for 6 h and dried overnight at 80 °C. The dried product was placed in a corundum crucible and calcined in a muffle furnace at 850 °C for 5 h with a heating rate of 10 °C min^{-1}. After calcination, the resulting yellow $NiNb_2O_6$ nanoparticles were thoroughly washed with hot deionized water to

remove any redundant salt. For comparison, $NiNb_2O_6$ microparticles ($NiNb_2O_6$-M) were synthesized using a traditional solid-state reaction method, where NiO and Nb_2O_5 powders with a molar ratio 1: 1 were mixed and calcined in air at 1300 °C for 4 h.

2.2.2 Preparation of $NiNb_2O_6$@C composites

mesophase pitch was used as carbon source. $NiNb_2O_6$ nanoparticles were mixed with varying proportions of mesophase pitch (5, 10, 20 wt%). The mixture was ground adequately and subsequently calcined in a tube furnace with flowing Ar atmosphere at 800 ℃ for 2 h with a heating rate of 10 ℃ min^{-1}. The resulting composites were designated as $NiNb_2O_6$@C-*x*, where *x* represents the weight percentage of mesophase pitch (5, 10 and 20 wt%).

2.3 Materials characterization

The X-ray diffraction (XRD) patterns of $NiNb_2O_6$ were acquired using a Bruker D8 diffractometer (Germany) with Cu-Kα radiation (λ=0.15406 nm) over a 2θ range of 5° to 90°. The chemical compositions and elemental valence states of the samples were analyzed by X-ray photoelectron spectroscopy (XPS, Thermo Scientific K-Alpha, America). Raman spectroscopy was conducted using a laser Horiba Lab RAM HR Evolution Raman spectrometer (Japan). The microstructure, elements distribution and crystal lattice of samples were examined by scanning electron microscopy (SEM, VEGA-3 from TESCAN Inc, China) equipped with energy dispersive spectroscopy (EDS) and transmission electron microscope (TEM, JEM-2010 from JEOL Inc, Japan). The in-situ X-ray diffraction (XRD) experiments were performed with a custom-designed in-situ XRD cell. The electrode material slurry was coated onto the copper mesh, with beryllium (Be) serving as an X-ray transmissive window. The cell was subjected to testing within a voltage range of 0.005 V to 3 V at a current density of 0.5 C.

2.4 Electrochemical measurements

The anodes for LIBs were prepared by blending the active material, carbon black as the conductive agent, and polyvinylidene fluoride (PVDF) as the binder in a mass ratio

of 7:2:1. This mixture was dispersed in 1-Methyl-2-pyrrolidinone (NMP) to form a homogeneous slurry The slurry was evenly coated onto copper foil and subsequently dried in a vacuum oven at 60 °C for 12 h. The dried copper foil was cut into small discs with a diameter of 12 mm, which served as the anode. A lithium tablet was used as the counter electrode and polypropylene film as the separator. The electrolyte consisted of 1 M $LiPF_6$ dissolved in a solvent mixture of ethylene carbonate (EC) and diethyl carbonate (DEC) in a voltage ratio of 1:1, with the addition of 5% fluoroethylene carbonate (FEC). The amount of electrolyte added to each cell was approximately 150 μL. The mass loading of the active material was 1.0~1.5 mg cm^{-2}. The half cells were assembled in an argon-filled glove box. The assembled batteries were subjected to galvanostatic discharge/charge tests using the Land battery test system (CT-2001A, Wuhan, China) at 25 °C, within the voltage range of 0.005~3 V. Cyclic voltammetry (CV) tests were performed with a CHI660E electrochemical workstation. Electrochemical impedance spectroscopy (EIS) measurements were also conducted on the electrochemical workstation, within a frequency range of 10^{-2}~10^{5} Hz. In this work, the C-rate used was defined as 1C = 236 mAh g^{-1}.

The full cells were assembled using the $NiNb_2O_6$@C electrode as the anode, which underwent prelithiation for five cycles in half cell. This anode was paired with a commercial $LiFePO_4$ electrode, composed of $LiFePO_4$, Super-P, and polyvinylidene fluoride (PVDF) in an 8:1:1 ratio. In the full cell assembly, the loading of anode material was about 1.0~1.3 mg cm^{-2}, with an anode/cathode mass ratio of approximately 1:1.05. The full cells were further assembled following the same procedure as for the half-cells.

3. Results and discussion

3.1 Preparation and characterization

The X-ray diffraction (XRD) patterns of $NiNb_2O_6$ and $NiNb_2O_6$@C were recorded (**Fig. 1a**). The prominent diffraction peaks at 24.66°, 30.50°, 36.35°, 53.97° and 64.83° correspond to the crystal planes (310), (311), (102), (621) and (332) of $NiNb_2O_6$, respectively. The results indicate that all the distinct diffraction peaks of the $NiNb_2O_6$

powders are well matched with the orthorhombic $NiNb_2O_6$ (PDF#72-0418), confirming the successful preparation of $NiNb_2O_6$. The XRD characteristic peaks of $NiNb_2O_6$ and $NiNb_2O_6$@C have no evident difference, implying that the carbon layer is amorphous and has no obvious characteristic peak. In addition, $NiNb_2O_6$ is reduced to Nb_2O_5 and Ni^0 when the mesophase pitch reaches 20 wt%, which is attributed to the reducibility of excess carbon (**Fig. S1**). For $NiNb_2O_6$@C-20%, several obvious diffraction peaks appear at 14.38°, 24.36°, 26.83°, 28.96°, 29.95°, 33.35°, 35.84°, 47.54° and 50.52°, corresponding to the crystal planes (002), ($\bar{2}$02), (200), (004), (030), (032), (202), ($\bar{2}$42) and (312) of Nb_2O_5, respectively. All the sharp diffraction peaks align with the standard card of Nb_2O_5 (PDF#19-0864). Additionally, three main characteristic peaks at diffraction angles of 44.49°, 51.87° and 76.34° match the standard card of Ni (PDF#87-0712). Therefore, when the mesophase pitch reaches 20 wt%, $NiNb_2O_6$ is reduced to Nb_2O_5 and metallic Ni^0, attributed to the reducibility of the excess carbon. Notably, $NiCl_2$ is added as the inorganic salt system on the basis of KCl and NaCl during the synthesis of $NiNb_2O_6$ by the molten salt method. This is because the addition of $NiCl_2$ can effectively promote the reaction ($NiO + Nb_2O_5 = NiNb_2O_6$) to synthesize pure $NiNb_2O_6$. It is confirmed that there are obvious characteristic peaks of Nb_2O_5 in the samples without adding $NiCl_2$ (**Fig. S2**). The XRD pattern of $NiNb_2O_6$-M (**Fig. S3**) synthesized via traditional solid-state reaction method proves the successful preparation of pure $NiNb_2O_6$, due to the diffraction peaks of $NiNb_2O_6$-M can be well indexed with the orthorhombic $NiNb_2O_6$ (PDF#72-0418). The crystal structure of $NiNb_2O_6$ belongs to the orthorhombic system (**Fig. 1b**). The oxygen atoms surround the niobium and nickel atoms to form an octahedral structure characterized by shared angles [32, 42]. Each niobium atom connects with six oxygen atoms, and each nickel atom is also bonded to six oxygen atoms. As a result, an organized layered arrangement with prominent channels is established, facilitating the rapid insertion/extraction of Li^+ ions. Benefiting from the distinctive crystal structure of nickel niobate, a solid foundation has been laid for its subsequent application in LIBs.

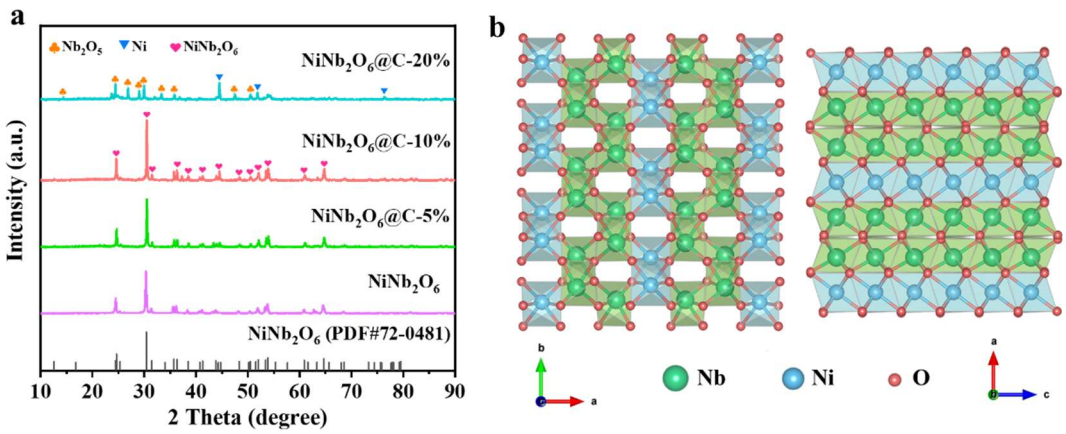

Fig. 1. (a) XRD patterns of $NiNb_2O_6$ and $NiNb_2O_6$@C. (b) Schematic diagrams of crystal structure of $NiNb_2O_6$.

The morphology characteristic, particle size, and microstructures of $NiNb_2O_6$ and $NiNb_2O_6$@C particles were analyzed by scanning electron microscopy (SEM) and transmission electron microscopy (TEM). $NiNb_2O_6$ exhibits nanometer-sized particles ranging from 200 to 500 nm (**Fig. 2a**). The introduction of an appropriate carbon coating has no significant effect on the morphology and dimension of $NiNb_2O_6$@C-10% (**Fig. 2b**). In the SEM images of $NiNb_2O_6$@C-5% (**Fig. S4**) and $NiNb_2O_6$@C-20% (**Fig. S5**), the significant changes in the morphology of $NiNb_2O_6$@C-20% are observed, due to the reduction of $NiNb_2O_6$. The SEM image (**Fig. S6**) depicts the morphology and particle size of $NiNb_2O_6$-M. The particles are about 2-5 μm in length and 0.5-2 μm in diameter, indicating a larger particle size compared to that of $NiNb_2O_6$ prepared by molten salt method. It is worth mentioning that the $NiNb_2O_6$ materials prepared by the simple molten salt method can achieve nano size without additional nano miniaturization. The small particle size not only shortens the ion transport path and promotes faster Li^+ transport, but also provides a larger specific surface area and more active sites. Several researchers have demonstrated by operando isothermal calorimetry that electrodes made of nanoparticles exhibit smaller instantaneous and time-averaged irreversible heat generation rates, highlighting smaller resistance loss and greater conductivity [43]. In consequence, a smaller particle size of the product confers greater advantages to the preparation method, implying that the molten salt method is superior

to the solid-state sintering method for preparing $NiNb_2O_6$.

The elemental mapping images of $NiNb_2O_6$@C-10% (**Fig. 2c-f**) in the rad dotted box further demonstrates the presence and uniform distribution of Ni, Nb, O, and C elements. The microstructure of the material was further analyzed by TEM (**Fig. S7**), where the high-resolution TEM image reveals distinct lattice spacings of 0.365 nm and 0.293 nm, corresponding respectively to the (310) and (311) crystallographic planes of $NiNb_2O_6$. The TEM (**Fig. 2g**) and HRTEM images of $NiNb_2O_6$@C-10% (**Fig. 2h**) depict the apparent lattice spacing of 0.254 nm, aligning with the (002) plane of $NiNb_2O_6$. Notably, a carbon layer derived from mesophase pitch has successfully coated on the surface of $NiNb_2O_6$ at a thickness of 2-5 nm. The selected area electron diffraction (SAED) pattern (**Fig. 2i**) demonstrates sharp diffraction spots at the orientation at [130] zone axis, indicating the orthorhombic phase of single-crystalline $NiNb_2O_6$.

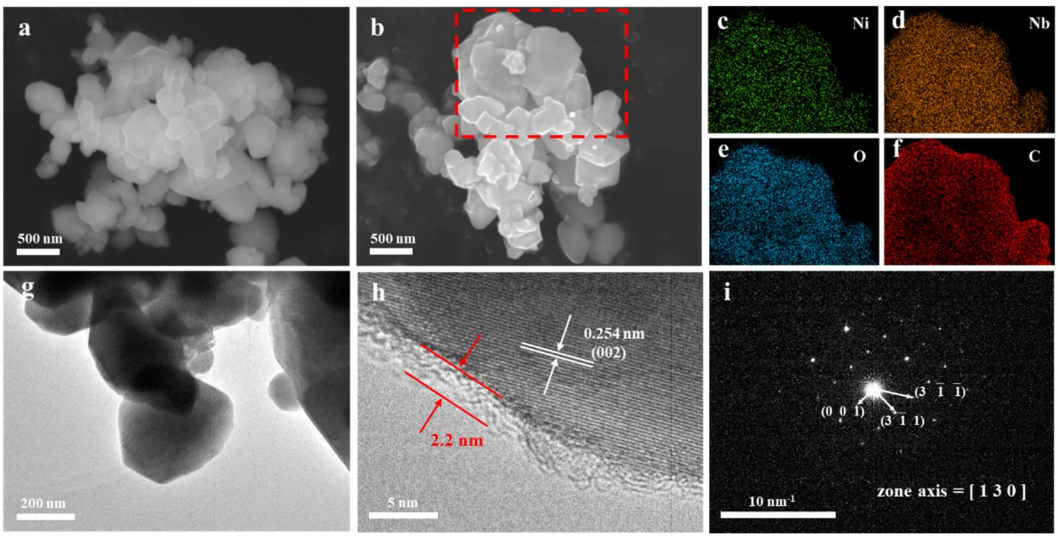

Fig. 2. SEM images of (a) $NiNb_2O_6$, and (b) $NiNb_2O_6$@C-10%. (c-f) The elemental mapping images of Ni, Nb, O, and C in $NiNb_2O_6$@C-10%. (g) TEM and (h) HRTEM images and (i) SAED pattern of $NiNb_2O_6$@C-10%.

The valence states and surface chemistry of $NiNb_2O_6$@C-10% powder was revealed by X-ray photoelectron spectroscopy (XPS). The survey spectra (**Fig. 3a**) show that Ni, Nb, O, and C elements coexist in $NiNb_2O_6$ and $NiNb_2O_6$@C-10%. In the XPS Nb spectra (**Fig. 3c**), two characteristic peaks of the Nb $3d_{5/2}$ and Nb $3d_{3/2}$ orbitals at 206.38

and 209.13 eV are triggered, which are related to the state of Nb^{5+} [44, 45]. The Ni 2p spectrum is fitted into Ni $2p_{3/2}$ and Ni $2p_{1/2}$ peaks at 855.69 and 873.47 eV, respectively, accompanied by two satellite peaks at 861.45 and 879.61 eV (**Fig. 3d**) [46, 47]. These peaks are originated from Ni^{2+} in nickel niobate, and no additional new phase is generated [32]. The O 1s spectrum (**Fig. 3e**) presents two distinct peaks at 529.88 and 532.08 eV, which are relevant to OH^- and O-M (M= Nb/Ni) bonds, respectively [48]. Furthermore, the characteristic peaks at 283.58 and 284.78 eV are ascribed to C 1s (**Fig. S8**) [49], underscoring the presence of carbon element in $NiNb_2O_6$@C-10%. The Raman spectrum further confirmed the presence of the carbon layer (**Fig. 3b**). Compared with $NiNb_2O_6$, $NiNb_2O_6$@C-10% appears obvious characteristic peaks at 1340 and 1600 cm^{-1}, which are identified as the disordered carbon (D-band) and graphitic carbon (G-band), respectively [50]. Other characteristic peaks prior to 1000 cm^{-1} are highly consistent between the $NiNb_2O_6$ and $NiNb_2O_6$@C-10%. The sharpest characteristic peak appearing at 879 cm^{-1} is associated with Nb-O stretching vibration in $NiNb_2O_6$. Moreover, other peaks at 638, 529, and 483 cm^{-1} correspond to the stretching and bending modes of Nb-O, Ni-O, and O-Nb-O, respectively. The peaks located at lower than 400 cm^{-1} are related to Nb-Nb stretching and Nb-O-Nb bending [34]. The results of Raman spectra verify the chemical bonds in $NiNb_2O_6$ and bear out the results of XRD and XPS, which demonstrate the successful preparation of the $NiNb_2O_6$ and the successful introduction of the carbon layer.

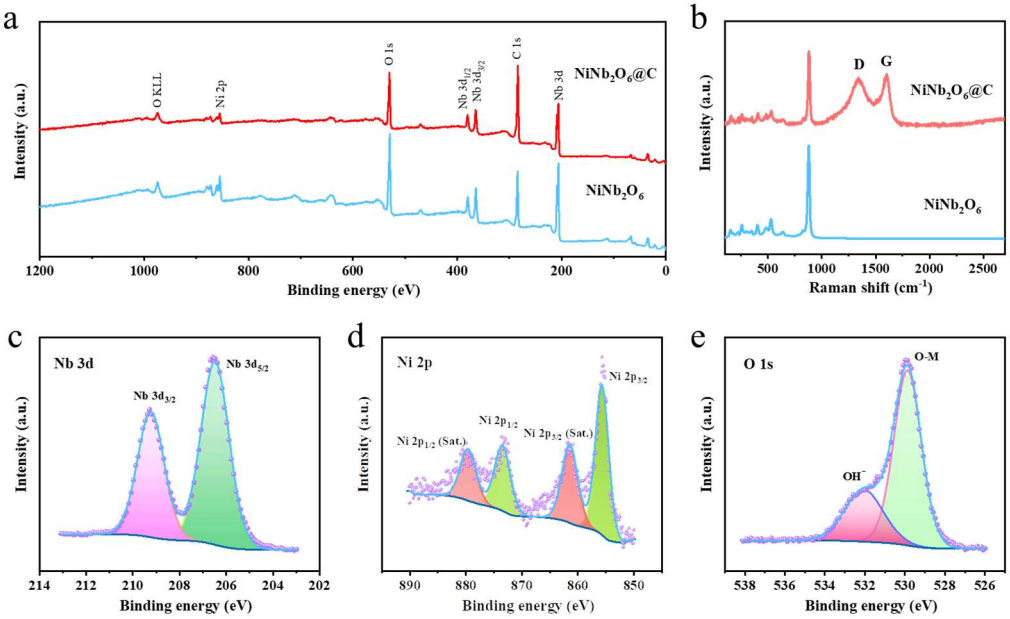

Fig. 3. (a) XPS survey spectra and (b) Raman spectra of $NiNb_2O_6$ and $NiNb_2O_6$@C. High-resolution XPS spectra of (c) Nb 3d, (d) Ni 2p, and (e) O 1s of $NiNb_2O_6$@C.

3.2 Electrochemical performance

The electrochemical properties of $NiNb_2O_6$ and $NiNb_2O_6$@C were evaluated in a half-cell configuration as anode materials for lithium-ion batteries. The cycle voltammetry (CV) curves of $NiNb_2O_6$@C-10% (**Fig. 4a**) for the first four cycles are recorded at a scan rate of 0.2 mV s^{-1} in a voltage window range between 0.005 and 3.0 V. Easy to see, the CV curve of the first circle is obviously different from others. In the first sweep, the three cathodic peaks are observed at 1.52 V, 0.95 V and 0.74V, which can be attributed to the redox couples of Nb^{5+}/Nb^{4+}, Nb^{4+}/Nb^{3+}, and Nb^{3+}/Nb^{2+}, respectively. In addition, the strong cathodic peak located at 0.19 V are ascribed to two aspects. First, a portion of Ni^{2+} in $NiNb_2O_6$ decomposed irreversibly into Ni atoms. Second, the formation of solid electrolyte interface (SEI) film occurred, leading to irreversible capacity loss. In subsequent cycles, a pair of redox peaks emerged at 1.77/1.54 V, indicative of the redox reactions of Nb^{5+}/Nb^{4+} [34, 51]. It is worth mentioning that the redox peaks of the second cycle are shifted relative to the third and fourth cycles, which is mainly due to the effect of incomplete reaction of the

electrochemical reconstruction process. The third and fourth cycles exhibit a remarkable consistency, reflecting the excellent reversibility during the cycling process. Furthermore, the CV curves of $NiNb_2O_6$ at 0.2 mV s^{-1} are shown (**Fig. S9**). It is notable that the cathodic peak intensity of $NiNb_2O_6$@C at 0.2 V is lower than that of $NiNb_2O_6$, suggesting that the carbon coating has a proper alleviating effect on the formation of SEI film and the entrapment of lithium ions.

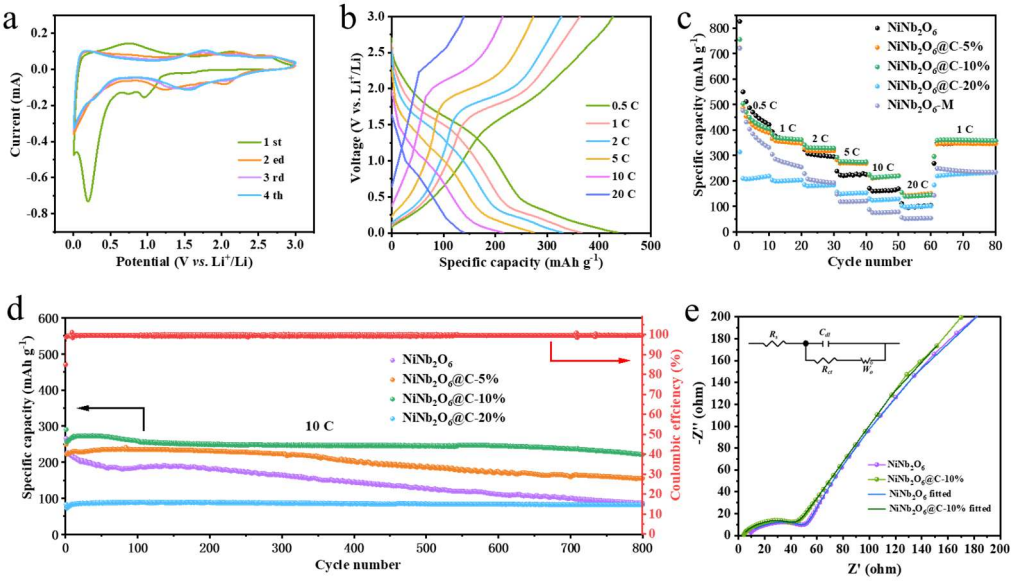

Fig. 4. (a) CV curves of $NiNb_2O_6$@C-10% at 0.2 mV s^{-1}. (b) GCD profiles of $NiNb_2O_6$@C-10% at different current densities. (c) Rate behavior and cycling performance (1 C) of $NiNb_2O_6$, $NiNb_2O_6$@C and $NiNb_2O_6$-M. (d) Long-term cycling performance of $NiNb_2O_6$ and $NiNb_2O_6$@C at 10 C. (e) EIS spectra of $NiNb_2O_6$ and $NiNb_2O_6$@C-10% obtained in a fully charged state with the equivalent circuit model.

The galvanostatic charge-discharge (GCD) curves of the $NiNb_2O_6$@C-10% at 0.5 C are presented (**Fig. S10**). The initial discharge and charge capacities of $NiNb_2O_6$@C-10% are 755.21 and 551.09 mAh g^{-1}, respectively. The corresponding initial Coulombic efficiency (ICE) stands at 72.97%, surpassing other previously reported niobium-based oxides anodes for LIBs [39, 52, 53]. Moreover, the Coulomb efficiency of the charging and discharging process at various current densities can reach more than 99%, demonstrating excellent electrochemical reversibility. The capacity of $NiNb_2O_6$@C-10% attenuates during the initial few cycles and stabilizes after the 5th cycle. Subsequent

cycles exhibit an enhanced Coulombic efficiency, reaching up to 98%. At higher current densities, the Coulomb efficiency can approach approximately 100%. At a low current density of 0.5 C, Li^+ gradually infiltrate into the $NiNb_2O_6$ material. But some lithium ions are trapped during the extraction process, leaving a certain amount of residual "dead lithium" within the material lattice after each cycle, resulting in the attenuation of the capacity in the next cycle. The results are consistent with the CV results. The GCD curves of $NiNb_2O_6$@C-10% are tested (**Fig. 4b**) at various current density from 0.5 C to 20 C. As the current density increases gradually, the shape of the GCD curves remains similar, highlighting the exceptional stability and excellent rate performance of the $NiNb_2O_6$@C-10% anode material. On the contrary, the GCD curves of $NiNb_2O_6$ (**Fig. S11**) express more capacity attenuation. The rate performances at different current densities (**Fig. 4c**) of $NiNb_2O_6$, $NiNb_2O_6$-M, and $NiNb_2O_6$@C composites are exhibited. At lower current density (0.5 C and 1 C), the specific capacity of $NiNb_2O_6$, $NiNb_2O_6$@C-5%, and $NiNb_2O_6$@C-10% have little variance. Nevertheless, as the current density escalates, a notable enhancement in rate performance becomes evident specifically in the case of $NiNb_2O_6$@C. The principal factor contributing to the improvement lies in the coating of mesophase pitch on the surface of $NiNb_2O_6$, which enhances the conductivity of the $NiNb_2O_6$ and promotes the diffusion kinetics of lithium-ions. The specific capacities of $NiNb_2O_6$@C-5% and $NiNb_2O_6$@C-10% are similar, while excessive carbon (as seen in $NiNb_2O_6$@C-20%) induces the reduction of $NiNb_2O_6$ to Nb_2O_5, resulting in a striking reduction of capacity. Impressively, $NiNb_2O_6$@C-10% displays the exceptional discharge specific capacities of 436.3, 366.2, 329.3, 274.6, 214.8, and 140.6 mAh g^{-1} at 0.5, 1, 2, 5, 10, and 20 C, respectively. When returning to 1 C, the specific capacity remains steadfast at 360 mAh g^{-1}, exhibiting outstanding reversible performance.

The cycle performances of $NiNb_2O_6$ and $NiNb_2O_6$@C are reflected (**Fig. 4d**) at 10 C. Under optimal conditions, $NiNb_2O_6$@C-10% demonstrates outstanding cycling performance, sustaining a capacity of 222.9 mAh g^{-1} even after 800 cycles. Notably, the capacity retention rate reaches an impressive 86.3%. In contrast, $NiNb_2O_6$@C-5% and $NiNb_2O_6$ exhibit lower capacity retentions of only 68.7% and 38.4%, respectively.

Therefore, an appropriate amount of mesophase pitch-derived carbon coating on $NiNb_2O_6$ plays a pivotal role in curbing the volume expansion during the charge/discharge cycling, thus contributing to the preservation of structural stability and ultimately leading to exceptional cycling stability. $NiNb_2O_6$-M at 10 C (**Fig. S12**) has a lower specific capacity (99.6 mAh g^{-1}) but can maintain a relatively consistent cycling performance, which is attributed to the unique structural characteristics inherent of nickel niobate itself. Electrochemical impedance spectroscopy (EIS) was employed to evaluate the diffusion of Li^+ in the electrode. The plots of both $NiNb_2O_6$ and $NiNb_2O_6$@C-10% (**Fig. 4e**) encompass a semicircle in the high-frequency region, corresponding to the charge-transfer resistance (R_{ct}). Simultaneously, an inclined line is evident in the low-frequency region, indicative of the Warburg impedance (W_o). This combination of impedance characteristics provides insights into the intricate lithium ions diffusion processes within the electrode. Both anodes present an identical EIS equivalent circuit model, encompassing R_s, R_{ct}, double layer capacitance (C_{dl}), and Warburg diffusion resistance (W_o). The fitted R_{ct} value for $NiNb_2O_6$@C-10% is lower than that of the $NiNb_2O_6$ electrode (44.2 Ω and 58.1 Ω, respectively), suggesting an accelerated interfacial Li^+ transfer and enhanced electrochemical kinetics. This also underscores the positive effects of carbon coating on the $NiNb_2O_6$ material. The augmentation in electrochemical performance benefits from the improved conductivity introduced by the carbon layer, which serves to expedite the rate of ion transfer. This outcome highlights the pivotal role of the carbon coating in promoting efficient Li^+ diffusion across the electrode-electrolyte interface.

To catch deeper insights into the Li^+ storage mechanism and reaction kinetics of $NiNb_2O_6$@C-10%, cyclic voltammetry (CV) was tested at different scanning rates (0.2, 0.4, 0.6, 0.8 and 1.0 mV s^{-1}, **Fig. 5a**). The CV curves unveil dominant reaction peak at 1.85/1.5 V in the charging and discharging process, corresponding to the transformation from Nb^{5+} to Nb^{4+}. The CV curves keep similar shapes at different scanning rates, reinforcing the stability and reversibility of the redox reaction in the $NiNb_2O_6$@C-10% electrode material. The Li^+ storage mechanism conforms to the following relationship formula between the peak current (i) and scan rate (v):

$$i = av^b \quad (1)$$

where a and b are constants. The dominant behavior of the electrochemical lithium storage is confirmed by calculating the b value. b equaling 0.5 indicates a process controlled by diffusion, while b equaling 1 signifies the capacitive behavior. The calculated b values of peaks 1 and 2 for anodic and cathodic peak (**Fig. 5b**) are 0.99 and 0.83, respectively, suggesting that the reaction process is primarily controlled by capacitance as the b values are in close to 1. The ratio of the capacitive and diffusion control contributions can be further quantified by the following equation:

$$i = k_1 v + k_2 v^{0.5} \quad (2)$$

where $k_1 v$ is assigned the pseudocapacitive contribution and $k_2 v^{0.5}$ stands for diffusion control contribution. The calculation results manifest that capacitive contribution is 69.37% at the scan rate of 1 mV s^{-1} (**Fig. 5c**), indicative of a pseudocapacitive dominated process. The corresponding pseudocapacitance contribution ratio of the capacitance content data from 0.2 to 0.8 mV s^{-1} gradually increases with rising sweep rates (**Fig. S13**). It is demonstrated that this intercalation charge storage process is not limited by lithium-ion diffusion but by surface processes. Moreover, the proportion of capacitance contribution and diffusion contribution at different scanning rates is depicts (**Fig. 5d**). Notably, the proportion of pseudocapacitance contribution escalates from 50.21% to 69.37% with the increase in scanning rate from 0.2 to 1.0 mV s^{-1}, thereby elucidating the pronounced disparity in rate performance.

Galvanostatic intermittent titration technique (GITT) was employed to further analyze the lithium-ion diffusion coefficients during the discharging and charging process (**Fig. S14**). GITT measurement was conducted at a current density of 1 C. The Li^+ diffusion coefficient (D_{Li^+}) can be determined by the following equation:

$$D_{Li^+} = \frac{4}{\pi\tau}\left(\frac{m_B V_m}{M_B S}\right)^2\left(\frac{\Delta E_s}{\Delta E_t}\right)^2 \quad (3)$$

where m_B and M_B are the mass and molecular weight of active materials, respectively, V_m is the molar volume, S stands for the electrode/electrolyte contact area, ΔE_s is the potential change caused by the pulse, and ΔE_t is the potential change caused by the constant current charge. The results demonstrate that the lithium-ion diffusion

coefficients (D_{Li^+}) of the $NiNb_2O_6$@C-10% electrode ranges from 1.15×10^{-12} cm^2 s^{-1} to 2.69×10^{-14} cm^2 s^{-1} during the discharge process and from 1.18×10^{-11} cm^2 s^{-1} to 3.35×10^{-12} cm^2 s^{-1} during the charge process. The improved Li^+ diffusion kinetics can be attributed to the favorable combination of factors, including the shortened Li^+ transport pathway between nanoparticles and the enhanced electrical conductivity facilitated by the carbon coating.

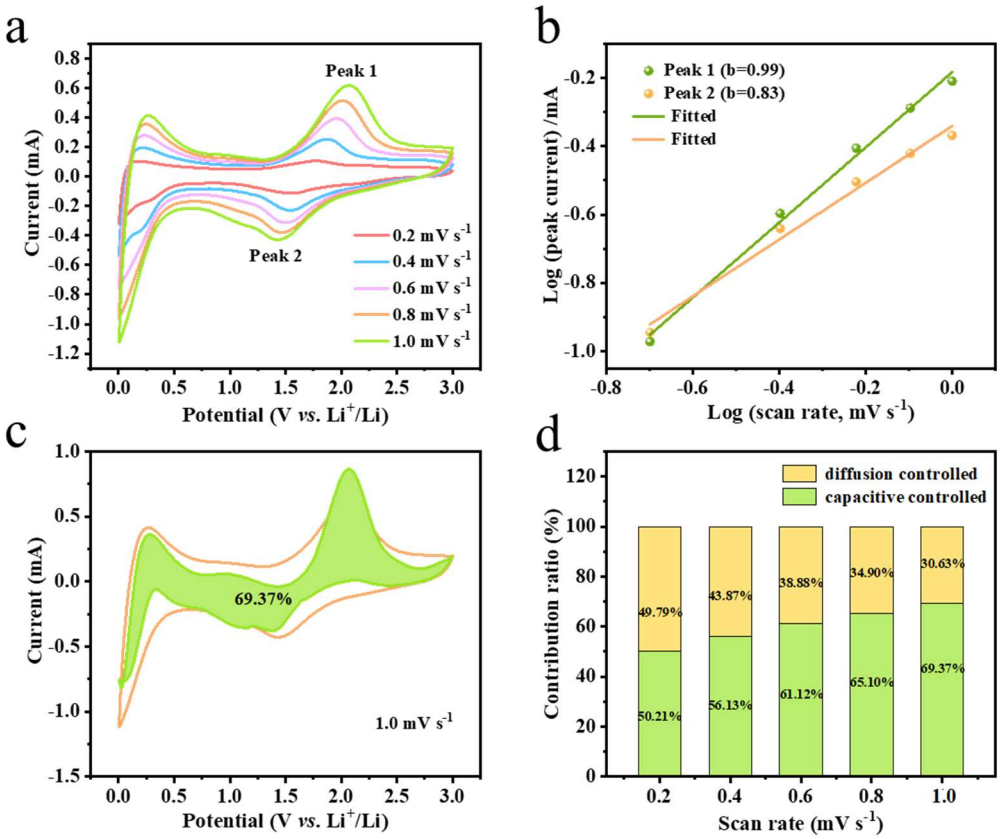

Fig. 5. (a) CV curves of $NiNb_2O_6$@C-10% at various scan rates from 0.2 to 1.0 mV s^{-1}. (b) Plots of logarithm current versus logarithm scan rate for $NiNb_2O_6$@C-10%. (c) Capacitive content for $NiNb_2O_6$@C-10% at a scan rate of 1.0 mV s^{-1}. (d) Capacitive contribution and diffusion contribution for $NiNb_2O_6$@C-10% at different scan rates.

3.3 Electrochemical mechanism

To enhance the understanding of the structural and morphological evolution in $NiNb_2O_6$ during insertion and extraction of Li^+, comprehensive in-situ XRD and ex-situ analyses were performed on $NiNb_2O_6$@C-10%. The in-situ XRD experiment of

$NiNb_2O_6$@C-10% anode involved collecting initial discharge/charge curves at a current density of 0.5 C within the range of 0.005 to 3 V. The in-situ XRD results (**Fig. 6a**) show that the characteristic peaks associated with the (310), (311), (102), (621) and (332) planes for $NiNb_2O_6$ (PDF#72-0418) gradually reduce and eventually fade away during the discharge process. Importantly, these diffraction peaks never recover in the subsequent charging process. A new and weak diffraction peak appears at 44.4°, which is attributed to Ni^0 (PDF#70-1849). This observed alteration suggests that Ni ions undergo substitution by Li ions during the lithiation process. It is worth mentioning that the most prominent peak of $NiNb_2O_6$ at 30.50°, corresponding to the (311) plane, demonstrates a clearly irreversible evolution (**Fig. 6b**). Following the first discharge/charge cycle, only the distinctive peaks of Ni^0 remain detectable, providing evidence that the irreversible reaction of $NiNb_2O_6$ occurs during the Li^+ insertion process. This further explains the comparatively inferior initial coulombic efficiency. It is a common occurrence for columbite-type niobates to undergo transformation into distinct metal oxides. Conversely, lamellar Nb_2O_5 functions as the host for the intercalation of lithium ions, ultimately leading to the formation of an amorphous phase denoted as $Li_xNb_2O_5$ [34]. In the in-situ XRD patterns, the diffraction peaks of Ni are relatively weak and not distinctly observable. This is due to the electrochemical reconstructed Ni particles are nanosized, resulting in inherently weak diffraction peaks. Moreover, the excessively high intensity of the diffraction peaks of Cu, Be, and BeO overshadow those of Ni and $NiNb_2O_6$, where the peaks of Cu, Be and BeO originate from the Cu foil in the electrode and the in-situ testing device, respectively. This phenomenon is unavoidable in in-situ XRD testing. In ex-situ XRD tests, we disassembled the half cells at different testing stages, scraped the active materials from the Cu foil to eliminate the interference from Cu peaks. Thus, the diffraction peaks with respect to Ni^0 can be observed in the absence of interference from other diffraction peaks. The discharge/charge curves of $NiNb_2O_6$@C-10% during the initial cycle at a current density of 0.5 C are presented alongside the corresponding ex-situ XRD patterns at various discharge/charge stages (**Fig. 6c**). Following the first complete discharge, the diffraction peaks associated with $NiNb_2O_6$ become indiscernible and new peaks of Ni^0

(PDF#70-1849) at 44.4° and 51.8° are recorded. Throughout the charging process, only the peaks of Ni^0 exist, and other phases exhibit characteristics of amorphous phase. Importantly, these results align completely with the in-situ XRD findings, confirming result consistency.

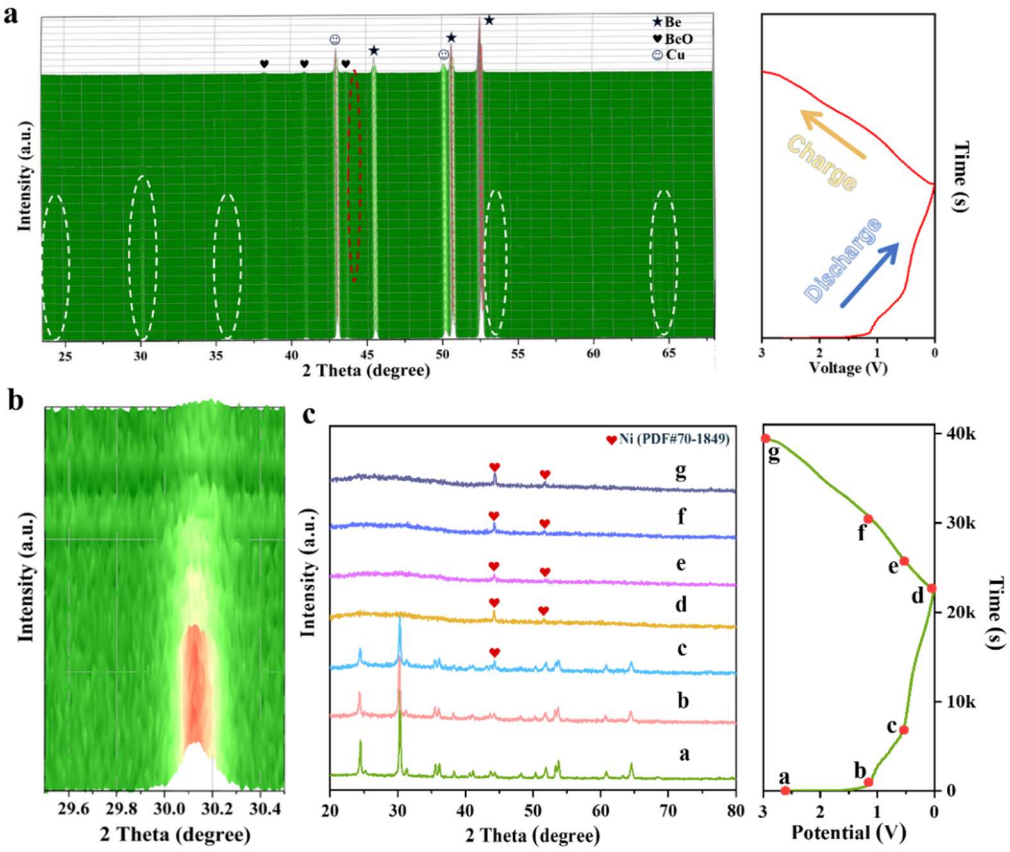

Fig. 6. (a) In-situ XRD patterns of $NiNb_2O_6$@C-10% with corresponding discharge/charge curves during the initial cycle within a voltage window of 0.005-3 V at 0.5 C. (b) In-situ XRD patterns of $NiNb_2O_6$@C-10% within the 2θ range of 29.5-30.5°. (c) Ex-situ XRD patterns of $NiNb_2O_6$@C-10% at various voltage stages.

Ex-situ XPS tests were performed to further provide additional evidence of the conversion mechanism during the initial cycle. The peaks originated from Nb 3d orbit (**Fig. 7a**) at 206.38 and 209.13 eV shift to lower binding energy corresponding to Nb^{4+} after discharge down to 0.005 V. Subsequently, these peaks revert to their initial positions after being charged to 3 V. This observation strongly reveals that the primary mechanism for lithium storage in $NiNb_2O_6$ involves a reversible Nb^{5+}/Nb^{4+} redox

reaction. Meanwhile, a new signal at 850.1 eV belonging to Ni^0 (**Fig. 7b**) emerges during discharge process and retains its stability throughout the whole cycle. This further proves that Ni^0 is irreversibly generated during the electrochemical process and lacks the activity to effectively bind with Li^+ [32, 34, 54]. Moreover, the Ni^{2+} peaks at 855.69 eV split into two peaks after discharge process, which may be ascribe to the formation of both NiO and Li_xNiO. Through in-situ and ex-situ characterizations of XRD and XPS, we have validated the electrochemical reconstruction process involving the formation of Ni^0 and amorphous Nb_2O_5 phase. The presence of Ni metal can improve the conductivity of the electrode material. Simultaneously, the lattice of amorphous Nb_2O_5 creates defects, thereby further promoting charge transfer. The XRD patterns of $NiNb_2O_6$@C-10% and $NiNb_2O_6$ (**Fig. 7c**) after 800 cycles illustrate the impact of mesophase pitch-derived carbon in the system. Notably, the characteristic peak of Ni^0 appears at 44.4° in the $NiNb_2O_6$@C-10% electrode after cycles. Therefore, it can be inferred that the surface carbon layer efficiently suppresses the exfoliation of superficial Ni^0. This phenomenon, in turn, bolster the electronic conductivity of active materials, thereby contributing to the superior rate performance and splendid cycling stability.

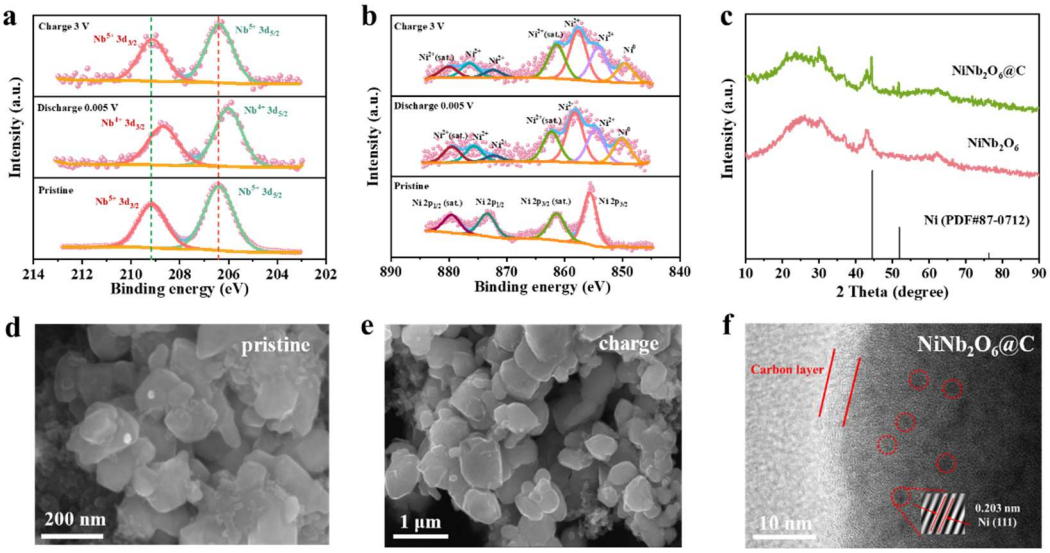

Fig. 7. (a) Nb 3d and (b) Ni 2p ex-situ XPS spectra of $NiNb_2O_6$@C-10% at pristine, discharged to 0.005 V, charged to 3 V in the first cycle. (c) XRD patterns of $NiNb_2O_6$@C-10% and $NiNb_2O_6$ after 800 cycles. (d) SEM images of $NiNb_2O_6$@C-10% before cycling and (e) after the initial charge. (f)

TEM image of $NiNb_2O_6$ after the initial charge.

In order to verify the effect of the carbon layer and Ni^0 on Li^+ transfer kinetics after cycling, the EIS curves were recorded (**Fig. S16**). Due to the presence of carbon layer, the overall conductivity of the electrode material experiences augmentation. After 800 cycles, two distinct semicircles can be observed on the EIS curves. The semicircle in the high frequency region is attributed to the interface contact resistance, which is correlated with the deposition of the interface layer on the electrode. The corresponding interface contact resistors of $NiNb_2O_6$ and $NiNb_2O_6$@C are 13.9 Ω and 8.5 Ω, respectively. The semicircle in the middle frequency region is attributed to the charge transfer resistance (R_{ct}). The R_{ct} of $NiNb_2O_6$@C is significantly lower than that of the $NiNb_2O_6$ electrode (213.3 Ω and 291.1 Ω, respectively), indicating that $NiNb_2O_6$@C has faster electrochemical reaction kinetics and emphasizes the positive effect of carbon coating. This conclusion is highly consistent with the conclusion of Fig. 4e.

Furthermore, ex-situ SEM and TEM examination were performed to visualize the morphological structure of the $NiNb_2O_6$@C-10% electrode material in various discharge/charge states. Strikingly, after a full cycle of Li^+ intercalation and deintercalation, the morphology of $NiNb_2O_6$@C-10% has no discernible change, proving its well-reserved structure stability after the irreversible conversion and the advantageous cycling stability (**Fig. 7d, e**). Additionally, the phase evolution during the lithiation/delithiation process was investigated by ex situ TEM after the first cycle (**Fig. 7f**). The TEM image of $NiNb_2O_6$@C displays clear lattice fringes with a spacing of 0.203 nm, aligning with the (111) crystal plane of Ni^0, which further proves the existence of Ni^0 and corresponds to the in-situ XRD results. Therefore, after electrochemical reconstruction, the initial niobate is transformed into metallic Ni and Nb_2O_5, thereby building a Mott-Schottky heterostructure. This novel structure featuring Mott-Schottky heterointerfaces are anticipating to enhance electron transport dynamics and speed up ion transport during lithium storage. Meanwhile, it is obviously observed that the carbon layer still remains intact on the surface of the material. It is noteworthy that the previously smooth particles have turned accidented, which can be ascribed to

the decoration of Ni^0 on the surface (**Fig. S17a**). In contrast to the SEM image of $NiNb_2O_6$ after 800 cycles (**Fig. S17b**), the morphology of nanoparticles keeps regular, which is consistent with the aforementioned in-situ XRD results.

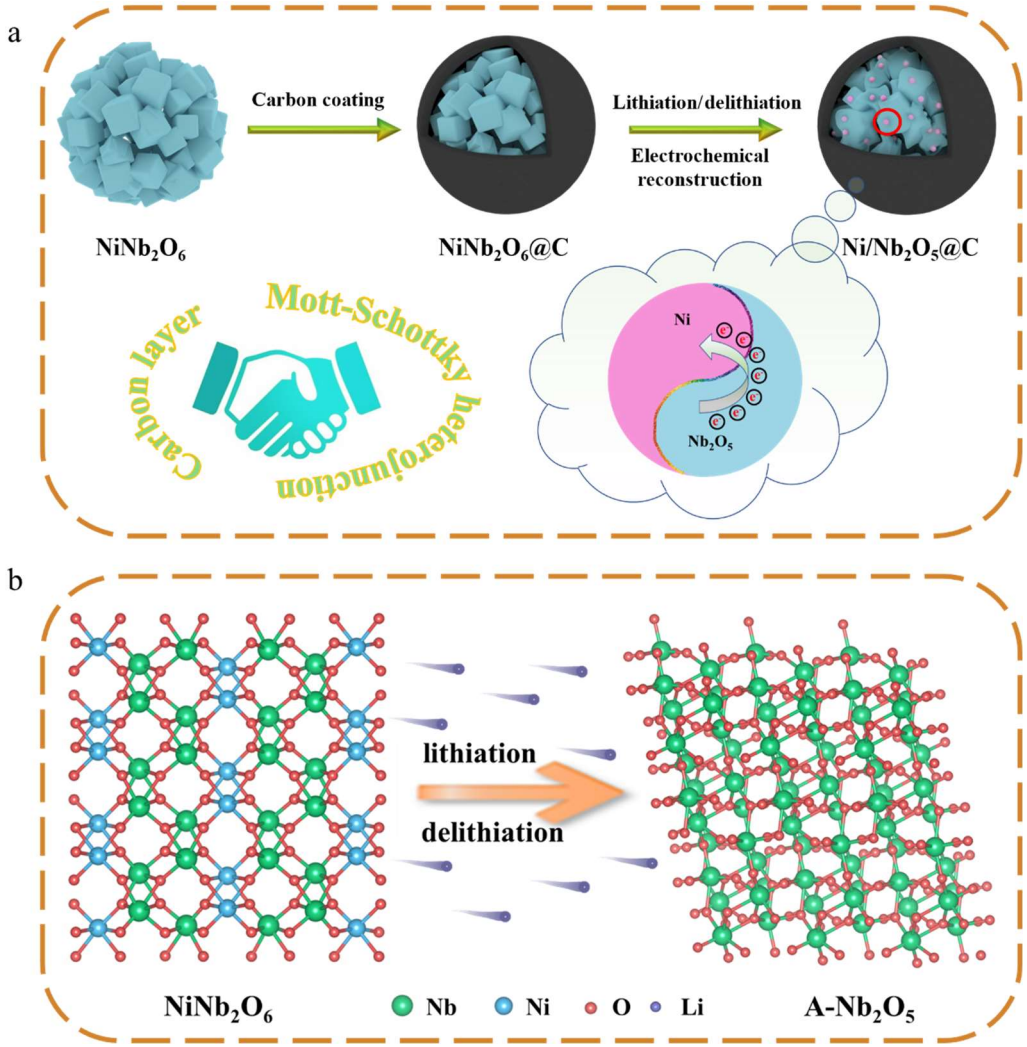

Fig. 8. (a) Schematic diagram of the reaction process and lithium storage mechanism. (b) Schematic diagram of the atomic-level structure for spontaneous electrochemical reconstruction after lithiation/delithiation.

The proposal schematic diagram of reactions and lithium storage mechanism is summarized (**Fig. 8a**). Firstly, $NiNb_2O_6$ prepared by molten salt method was modified with carbon coating to obtain $NiNb_2O_6$@C composite material. The carbon layer not only serves as a conductive network to improve the overall conductivity of the material,

but also regards as a protective barrier for Ni^0 to inhibit the detachment of Ni^0 from the material surface. Furthermore, $NiNb_2O_6$@C undergoes an intrinsic electrochemical reconstruction into Ni/Nb_2O_5@C during the process of lithiation and delithiation, accompanied by the generation of Mott-Schottky heterojunctions. The Fermi energy level difference between the metal and the semiconductor is utilized to induce charge separation at the interface and to accelerate electron transport in the LIBs. Therefore, the synergistic effects of the dual conductive interfaces, which consists of the carbon layer and the Mott-Schottky heterojunction between amorphous Nb_2O_5 and metallic Ni, contribute to the excellent electrochemical performance.

The atomic-level configuration arises from the spontaneous electrochemical reconstruction after lithiation/delithiation is illustrated (**Fig. 8b**). The initial orthogonal phase of $NiNb_2O_6$ is transformed into an amorphous phase of Nb_2O_5 (A-Nb_2O_5) and metallic Ni. The precipitation of Ni^0 after electrochemical reconstruction not only enhances the conductivity of the material to a certain extent, but also constructs a Mott-Schottky heterostructure due to the intimate interacts with the semiconductor Nb_2O_5. The amorphous lattice structure of A-Nb_2O_5 characterized by its disordered atomic arrangement can enhance the intrinsic conductivity of the material and promote charge transfer [55, 56]. This is particularly conducive to the reversible redox reaction between Nb^{5+} and Nb^{4+} that takes place during subsequent lithium storage processes.

3.4 Full cell electrochemical performance

To further validate the practical application potential of $NiNb_2O_6$@C, we constructed a full cell by paring the cathode material $LiFePO_4$ and the anode material $NiNb_2O_6$@C. This allowed us to thoroughly assess the electrochemical performance, the schematic illustration is provided in (**Fig. 9a**). The GCD curves of the $LiFePO_4$ || $NiNb_2O_6$@C full cell at 0.5 C are presented (**Fig. 9b**). In the initial stages of the charging and discharging process, the capacity experiences a gradual increase attributed to the activation of the electrode material. Subsequently, the capacity stabilizes after the third cycle. The charge/discharge plots and rate performance of $LiFePO_4$ || $NiNb_2O_6$@C at different current densities are depicted (**Fig. 9c, d**). The specific capacities are 124.5,

116.8, 108.5, 93.9, 77.8 and 56.8 mAh g^{-1} at 0.5, 1, 2, 5, 10 and 20 C, respectively. Remarkably, when returned to 1 C, the specific capacity can reach 113.5 mAh g^{-1} and maintain impressive stability. The results reveal that the $LiFePO_4$ || $NiNb_2O_6$@C full cell exhibits an excellent rate performance for fast-charging application. Moreover, the $LiFePO_4$ || $NiNb_2O_6$@C full cell emerges outstanding long cycling life, maintaining the specific capacity of 85.5 mAh g^{-1} at 5 C after 500 cycles (**Fig. 9e**) and a remarkably coulombic efficiency of 99.65%. It is noteworthy that the specific capacity increased initially and remained stable after 30 cycles. This probably due to that the spontaneous electrochemical reconstruction of $NiNb_2O_6$@C anode during the initial charging and discharging process, resulting in a change in the active composition of the anode. The generated metallic Ni and amorphous Nb_2O_5 form a Mott-Schottky heterostructure, which accelerates electron transport. The electrochemical reconstruction alters the active composition of the anode, allowing the material to achieve a higher discharge specific capacity during this activation process and subsequently reach a steady state. The practical viability of the $LiFePO_4$ || $NiNb_2O_6$@C full cell in daily life was assessed **(Fig. 9f)**, proving that LED lights designed with the "WUST" patterns can be successfully lit.

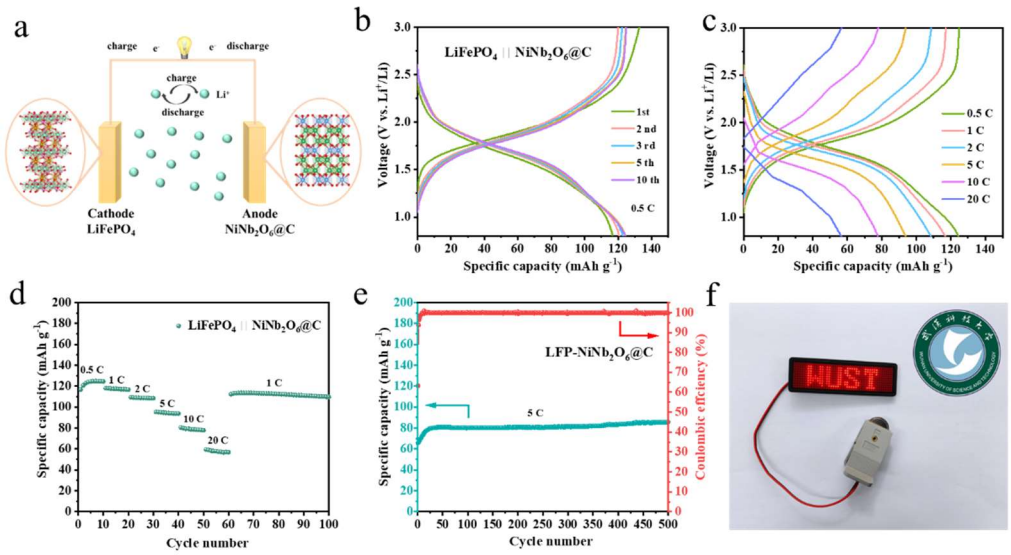

Fig. 9. (a) Schematic illustration of the fast charging/discharging full cell with $NiNb_2O_6$@C as the anode and $LiFePO_4$ as the cathode. (b) GCD cycles of the $LiFePO_4$ || $NiNb_2O_6$@C full cell at 0.5 C. (c) GCD curves of the $LiFePO_4$ || $NiNb_2O_6$@C full cell at various rates. (d) Rate performance and

(e) Cycling performance at 5 C of the $LiFePO_4$ || $NiNb_2O_6$@C full cell. (f) A photograph of the $LiFePO_4$ || $NiNb_2O_6$@C full cell lighting up the LED plates.

4. Conclusion

In summary, $NiNb_2O_6$ was successfully synthesized through molten salt method as an anode material for lithium-ion batteries. This approach boasts distinct advantages, including its simple operation, low calcination temperature (850 °C) and production of small particle size (200-500 nm). To address the inherent poor electrical conductivity of the $NiNb_2O_6$, we choose to modify a uniform carbon layer derived from mesophase pitch on the surface of the $NiNb_2O_6$ particles. The incorporated carbon layer serves a dual purpose in enhancing the properties of the composites, which not only establishes a conductive network to improve the conductivity of the materials, but also functions as a protective layer to prevent the stripping of the internal materials. During the charging/discharging process, $NiNb_2O_6$@C undergoes spontaneous electrochemical reconstruction, transforming into metallic Ni and amorphous Nb_2O_5. The presence of carbon layer effectively inhibits the stripping of Ni^0 on the surface, thus further enhancing the electronic conductivity of active materials. Furthermore, the interaction between Ni metal and Nb_2O_5 semiconductor gives rise to the creation of a Mott-Schottky heterostructure, which accelerates electron transport. The synergistic effects of the outer carbon layer and the Mott-Schottky heterostructure result in excellent electrochemical performance. Therefore, this work not only provides a simple synthetic method to prepare $NiNb_2O_6$ for large-scale production, but also designs an optimization strategy for the development of new generation energy materials.

Declaration of Competing Interests

The authors declare that they have no known competing interests.

Acknowledgments

This work was supported by the National Natural Science Foundation of China (grant numbers 22372127 and 52002296) and Supported by State Key Laboratory of Heavy Oil Processing (grant number WX20230152). The authors gratefully acknowledge the Analytical & Testing Center of Wuhan University of Science and Technology for the help on XPS analysis.

References

[1] Z. Zhu, T. Jiang, M. Ali, Y. Meng, Y. Jin, Y. Cui, W. Chen, Rechargeable batteries for grid scale energy storage, Chem. Rev. 122 (2022) 16610-16751.

[2] L. Tan, J. Wu, Y. Guan, Y. Jin, Z. Xu, H. Zhu, Q. Zhang, X. Li, Z. Dong, Y. Cong, Dual conductive confinement effects on enhancing Li-ion storage of NaV_6O_{15}@VO_2(M)@V_2C heterojunction, J. Alloys Compd. 964 (2023) 171242.

[3] F. Duffner, N. Kronemeyer, J. Tübke, J. Leker, M. Winter, R. Schmuch, Post-lithium-ion battery cell production and its compatibility with lithium-ion cell production infrastructure, Nat. Energy 6 (2021) 123-134.

[4] Y. Guan, R. Zhao, K. Li, K. Chen, H. Zhu, X. Li, Q. Zhang, N. Yang, Z. Dong, G. Yuan, Y. Li, Y. Cong, Tailoring surface chemistry of MXenes to boost initial coulombic efficiency for lithium storage, Appl. Surf. Sci. 612 (2023) 155875.

[5] C.Y. Wang, T. Liu, X.G. Yang, S. Ge, N.V. Stanley, E.S. Rountree, Y. Leng, B.D. McCarthy, Fast charging of energy-dense lithium-ion batteries, Nature 611 (2022) 485-490.

[6] C.D. Quilty, D. Wu, W. Li, D.C. Bock, L. Wang, L.M. Housel, A. Abraham, K.J. Takeuchi, A.C. Marschilok, E.S. Takeuchi, Electron and ion transport in lithium and lithium-ion battery negative and positive composite electrodes, Chem. Rev. 123 (2023) 1327-1363.

[7] P. Barnes, Y. Zuo, K. Dixon, D. Hou, S. Lee, Z. Ma, J.G. Connell, H. Zhou, C. Deng, K. Smith, E. Gabriel, Y. Liu, O.O. Maryon, P.H. Davis, H. Zhu, Y. Du, J. Qi, Z. Zhu, C. Chen, Z. Zhu, Y. Zhou, P.J. Simmonds, A.E. Briggs, D. Schwartz, S.P. Ong, H. Xiong, Electrochemically induced amorphous-to-rock-salt phase transformation in niobium oxide electrode for Li-ion batteries, Nat. Mater. 21 (2022) 795-803.

[8] Q. Xie, Y. Guan, Z. Xu, H. Zhu, Y. Jin, Q. Zhang, Z. Dong, G. Yuan, X. Li, Y. Cong, Dual interfaces and confinements on $Fe_2N@Fe_3O_4/VN$ heterojunction toward high-efficient lithium storage, J. Colloid Interface Sci. 650 (2023) 798-806.

[9] K. Chen, Y. Guan, L. Tan, H. Zhu, Q. Zhang, J. Guo, Z. Dong, G. Yuan, X. Li, Y. Cong, Atomically selective oxidation of (Ti,V) MXene to construct TiO_2@TiVCT heterojunction for high-performance Li-ion batteries, Appl. Surf. Sci. 617 (2023) 156575.

[10] Y. Han, B. Liu, Z. Xiao, W. Zhang, X. Wang, G. Pan, Y. Xia, X. Xia, J. Tu, Interface issues of lithium metal anode for high-energy batteries: Challenges, strategies, and perspectives, InfoMat 3 (2021) 155-174.

[11] H. Zhang, Y. Yang, H. Xu, L. Wang, X. Lu, X. He, $Li_4Ti_5O_{12}$ spinel anode: Fundamentals and advances in rechargeable batteries, InfoMat 4 (2021) 155-174.

[12] Z. Su, S. Li, L. Ma, T. Liu, M. Li, T. Wu, Q. Zhang, C. Dong, C. Lai, L. Gu, J. Lu, F. Pan, S. Zhang, Quenching-induced defects liberate the latent reversible capacity of lithium titanate anode, Adv. Mater. 35 (2023) e2208573.

[13] T.-F. Yi, H.M.K. Sari, X. Li, F. Wang, Y.-R. Zhu, J. Hu, J. Zhang, X. Li, A review of niobium oxides based nanocomposites for lithium-ion batteries, sodium-ion batteries and supercapacitors, Nano Energy 85 (2021) 105955.

[14] H. Ding, Z. Song, H. Zhang, H. Zhang, X. Li, Niobium-based oxide anodes toward fast and safe energy storage: A review, Mater. Today Nano 11 (2020) 100082.

[15] Y. Zheng, W. Qiu, L. Wang, J. Liu, S. Chen, C. Li, Triple conductive wiring by electron doping, chelation coating and electrochemical conversion in fluffy Nb_2O_5 anodes for fast-charging Li-ion batteries, Adv. Sci. 9 (2022) e2202201.

[16] J. Meng, Q. He, L. Xu, X. Zhang, F. Liu, X. Wang, Q. Li, X. Xu, G. Zhang, C. Niu, Z. Xiao, Z. Liu, Z. Zhu, Y. Zhao, L. Mai, Identification of phase control of carbon-confined Nb_2O_5 nanoparticles toward high-performance lithium storage, Adv. Energy Mater. 9 (2019) 1802695.

[17] F. Liu, Z. Zhu, Y. Chen, J. Meng, H. Wang, R. Yu, X. Hong, J. Wu, Dense T-Nb_2O_5/carbon microspheres for ultrafast-(dis)charge and high-loading lithium-ion

batteries, ACS Appl. Mater. Interfaces 14 (2022) 49865-49874.
[18] X. Ding, H. Huang, Q. Huang, B. Hu, X. Li, X. Ma, X. Xiong, Doping sites modulation of T-Nb_2O_5 to achieve ultrafast lithium storage, J. Energy Chem. 77 (2023) 280-289.
[19] X. Han, P.A. Russo, N. Goubard-Bretesché, S. Patanè, S. Santangelo, R. Zhang, N. Pinna, Exploiting the condensation reactions of acetophenone to engineer carbon-encapsulated Nb_2O_5 nanocrystals for high-performance Li and Na energy storage systems, Adv. Energy Mater. 9 (2019) 1902813.
[20] C. Yang, D. Ma, J. Yang, M. Manawan, T. Zhao, Y. Feng, J. Li, Z. Liu, Y.W. Zhang, R.B. Von Dreele, B.H. Toby, C.P.d.L. Albarrán, J.H. Pan, Crystallographic insight of reduced lattice volume expansion in mesoporous Cu^{2+}-doped $TiNb_2O_7$ microspheres during Li^+ insertion, Adv. Funct. Mater. 33 (2023) 2212854.
[21] R. Qian, H. Lu, T. Yao, F. Xiao, J.-W. Shi, Y. Cheng, H. Wang, Hollow $TiNb_2O_7$ nanospheres with a carbon coating as high-efficiency anode materials for lithium-ion batteries, ACS Sustain. Chem. & Eng. 10 (2021) 61-70.
[22] Y. Sui, J. Guo, Z. Li, F. Jiang, X. Xia, H. Geng, Q. Liu, B. Wei, X. Zuo, Kinetics modulation of titanium niobium oxide via hierarchical MXene coating for high-rate and high-energy density lithium-ion half/full batteries, Appl. Surf. Sci. 576 (2022) 151890.
[23] X. Jin, Y. Deng, H. Tian, M. Zhou, W. Tang, H. Dong, X. Zhang, R. Liu, Homovalent doping: An efficient strategy of the enhanced $TiNb_2O_7$ anode for lithium-ion batteries, Green Energy & Environ. (2023) https://doi.org/10.1016/j.gee.2023.01.007.
[24] Y. Yang, J. Huang, Z. Cao, Z. Lv, D. Wu, Z. Wen, W. Meng, J. Zeng, C.C. Li, J. Zhao, Synchronous manipulation of ion and electron transfer in Wadsley-Roth phase Ti-Nb oxides for fast-charging lithium-ion batteries, Adv. Sci. 9 (2022) e2104530.
[25] S. Shi, Y. Tang, G. Wang, W. Yu, G. Wan, L. Wu, Z. Deng, G. Wang, Multiple reinforcement effect induced by gradient carbon coating to comprehensively promote lithium storage performance of $Ti_2Nb_{10}O_{29}$, Nano Energy 96 (2022) 107132.
[26] Y. Lian, Y. Zheng, Z. Wang, Y. Hu, J. Zhao, H. Zhang, Hollow ppy@ $Ti_2Nb_{10}O_{29}$-

$_x$@NC bowls: A stress–release structure with vacancy defects and coating interface for Li capacitor, Chem. Eng. J. 454 (2023) 140287.

[27] M. Qi, M. Hu, J. Xu, X. Yuan, Z. Zhang, Smart construction of $Ti_2Nb_{10}O_{29}$ /carbon nanofiber core-shell composite arrays as anode materials for lithium-ion batteries, J. Alloy. Compd. 886 (2021) 161146.

[28] X. Xia, S. Deng, S. Feng, J. Wu, J. Tu, Hierarchical porous $Ti_2Nb_{10}O_{29}$ nanospheres as superior anode materials for lithium ion storage, J. Mater. Chem. A 5 (2017) 21134-21139.

[29] W. Utetiwabo, M. Khurram Tufail, C. Zeng, L. Zhou, L. Yang, Z. Hua, J. Zeng, P. Yu, R. Shao, W. Yang, Graphite foam as carbon-based footprint for in-situ fabrication of Ti^{3+}-doped titanium niobium oxide ($Ti_2Nb_{10}O_{29}$) nanocrystal for high-rate performance lithium-ion batteries, J. Colloid Interface Sci. 623 (2022) 1015-1026.

[30] L. Yang, X. Zhu, X. Li, X. Zhao, K. Pei, W. You, X. Li, Y. Chen, C. Lin, R. Che, Conductive copper niobate: Superior Li^+-storage capability and novel Li^+-transport mechanism, Adv. Energy Mater. 9 (2019) 1902174.

[31] X. Cai, H. Yan, Z. Yang, W. Li, H. Yu, L. Yan, L. Zhang, M. Shui, Y. Cui, J. Shu, Copper niobate nanowires boosted by a N, S co-doped carbon coating for superior lithium storage, Dalton Trans. 50 (2021) 11030-11038.

[32] R. Xia, K. Zhao, L.Y. Kuo, L. Zhang, D.M. Cunha, Y. Wang, S. Huang, J. Zheng, B. Boukamp, P. Kaghazchi, C. Sun, J.E. ten Elshof, M. Huijben, Nickel niobate anodes for high rate lithium-ion batteries, Adv. Energy Mater. 12 (2021) 2102972.

[33] Y. De Luna, N. Bensalah, Mechanochemical synthesis of orthorhombic nickel niobate ($NiNb_2O_6$) as a robust and fast charging anode material for lithium-ion batteries, ACS Appl. Energy Mater. 5 (2022) 7443-7457.

[34] H. Zhang, X. Zhang, Y. Gao, K. Zhu, J. Yan, K. Ye, K. Cheng, G. Wang, D. Cao, Rational design of N-doped carbon coated $NiNb_2O_6$ hollow nanoparticles as anode for Li-ion capacitor, Appl. Surf. Sci. 532 (2020) 147436.

[35] X. Liu, N. Fechler, M. Antonietti, Salt melt synthesis of ceramics, semiconductors and carbon nanostructures, Chem. Soc. Rev. 42 (2013) 8237-65.

[36] S. Zhao, J. Lian, S. Zhang, Y. Cui, G. Li, Y. Wang, H. Li, Molten salt synthesis of

submicron $NiNb_2O_6$ anode material with ultra-high rate performance for lithium-ion batteries, Chem. Eng. J. 461 (2023) 141997.

[37] J. Ma, X. Guo, H. Xue, K. Pan, C. Liu, H. Pang, Niobium/tantalum-based materials: Synthesis and applications in electrochemical energy storage, Chem. Eng. J. 380 (2020) 122428.

[38] G. Zhu, W. Jiao, Q. Li, Y. Zhao, X. Liu, R. Che, Conductivity optimization via intertwined CNTs between $TiNb_2O_7$@C microspheres for a superior performance Li-ion battery anode, J. Colloid Interfaces Sci. 607 (2022) 1103-1108.

[39] Y. Zhang, Y. Tang, L. Liu, Y. Gao, C. Zhu, X. Bai, X. Wang, $TiNbO_{2+2.5x}$ (x=2, 5, 6)/C hybrid nanotubes with enhanced kinetics for high-performance lithium anodes, Electrochim. Acta 410 (2022) 139862.

[40] Y. S. Hu, P. Adelhelm, B. M. Smarsly, S. Hore, M. Antonietti, J. Maier, Synthesis of hierarchically porous carbon monoliths with highly ordered microstructure and their application in rechargeable lithium batteries with high-rate capability, Adv. Funct. Mater. 17 (2007) 1873-1878.

[41] P. Zhai, J. Qin, L. Guo, N. Zhao, C. Shi, E.-Z. Liu, F. He, L. Ma, J. Li, C. He, Smart hybridization of $Sn_2Nb_2O_7/SnO_2$@3D carbon nanocomposites with enhanced sodium storage performance through self-buffering effects, J. Mater. Chem. A 5 (2017) 13052-13061.

[42] R. Wichmann, Synthese und untersuchung von $NiNb_2O_6$-Einkristallen mit columbit- und rutilstruktur, Zeitschrift für anorganische und allgemeine Chemie 503 (1983) 101-105.

[43] Y. Zhou, E. Le Calvez, S.W. Baek, M. Frajnkovič, C. Douard, E. Gautron, O. Crosnier, T. Brousse, L. Pilon, Effect of particle size on thermodynamics and lithium ion transport in electrodes made of $Ti_2Nb_2O_9$ microparticles or nanoparticles, Energy Storage Mater. 52 (2022) 371-385.

[44] D. Cao, Z. Yao, J. Liu, J. Zhang, C. Li, H-Nb_2O_5 wired by tetragonal tungsten bronze related domains as high-rate anode for Li-ion batteries, Energy Storage Mater. 11 (2018) 152-160.

[45] M.V. Cagnoli, A.M. Alvarez, N.G. Gallegos, J.F. Bengoa, C.D.D. de Souza, M. Schmal, S.G. Marchetti, Mössbauer and XPS spectroscopies studies of SMSI effect on Fe/Nb_2O_5 catalysts for the Fischer–Tropsch synthesis, Appl. Catal. A 326 (2007) 113-119.

[46] T. Xiao, F. Chen, W. Zhou, P. Che, S. Wang, X. Chen, X. Tan, P. Xiang, L. Jiang, X. Chen, Ni-Bi-S nanosheets/Ni foam as a binder-free high-performance electrode for asymmetric supercapacitors, Chem. Eng. J. 378 (2019) 122162.

[47] J. Wang, X. Ge, L. Shao, J. Zhang, D. Peng, G. Zou, H. Hou, W. Deng, S. Xu, X. Ji, W. Zhang, Reaction-driven transformation of Ni/NiO hybrid structure into Ni single atoms, Mater. Today Energy 17 (2020) 100436.

[48] H.-Q. Wang, X.-P. Fan, X.-H. Zhang, Y.-G. Huang, Q. Wu, Q.-C. Pan, Q.-Y. Li, In situ growth of NiO nanoparticles on carbon paper as a cathode for rechargeable Li–O_2 batteries, RSC Advances 7 (2017) 23328-23333.

[49] R. Qian, C. Yang, D. Ma, K. Li, T. Feng, J. Feng, J.H. Pan, Robust lithium storage of block copolymer-templated mesoporous $TiNb_2O_7$ and $TiNb_2O_7$@C anodes evaluated in half-cell and full-battery configurations, Electrochimica Acta 379 (2021) 138179.

[50] Z. Zheng, H.-H. Wu, H. Liu, Q. Zhang, X. He, S. Yu, V. Petrova, J. Feng, R. Kostecki, P. Liu, D.-L. Peng, M. Liu, M.-S. Wang, Achieving fast and durable lithium storage through amorphous FeP nanoparticles encapsulated in ultrathin 3D P-doped porous carbon nanosheets, ACS Nano 14(8) (2020) 9545-9561.

[51] X. Wang, G. Shen, Intercalation pseudo-capacitive $TiNb_2O_7$@carbon electrode for high-performance lithium ion hybrid electrochemical supercapacitors with ultrahigh energy density, Nano Energy 15 (2015) 104-115.

[52] M. Liang, Y. Huang, Y. Lin, G. Liang, C. Huang, L. Chen, J. Li, Q. Feng, C. Lin, Z. Huang, Micro-nano structured VNb_9O_{25} anode with superior electronic conductivity for high-rate and long-life lithium storage, J. Mater. Sci.Technol. 83 (2021) 66-74.

[53] L. Qin, Y. Liu, S. Zhu, D. Wu, G. Wang, J. Zhang, Y. Wang, L. Hou, C. Yuan, Formation and operating mechanisms of single-crystalline perovskite $NaNbO_3$ nanocubes/few-layered Nb_2CT_x MXene hybrids towards Li-ion capacitors, J. Mater. Chem. A 9 (2021) 20405-20416.

[54] M.Y. Yang, S. Kim, K. Kim, W. Cho, J.W. Choi, Y.S. Nam, Role of ordered Ni atoms in Li layers for Li-rich layered cathode materials, Adv. Funct. Mater. 27 (35) (2017) 1700982.

[55] S. Zhang, J. Hwang, K. Matsumoto, R. Hagiwara, In situ orthorhombic to amorphous phase transition of Nb_2O_5 and its temperature effect on pseudocapacitive behavior, ACS Appl. Mater. Interfaces 14 (2022) 19426-19436.

[56] X. Zhang, J. Wang, X. Wang, Y. Li, Y. Zhao, Z. Bakenov, G. Li, 3D ordered macroporous amorphous Nb_2O_5 as anode material for high-performance sodium-ion batteries, Appl. Surf. Sci. 567 (2021) 150862.